SANDIA REPORT
SAND2019-11256
Printed September 2019

Sandia National Laboratories

Integrated Geomechanics and Geophysics in Induced Seismicity: Mechanisms and Monitoring

Hongkyu Yoon, Michelle Williams, Kyung Won Chang, J. Eric Bower, Laura Pyrak-Nolte, and Antonio Bobet

Prepared by
Sandia National Laboratories
Albuquerque, New Mexico
87185 and Livermore,
California 94550

Issued by Sandia National Laboratories, operated for the United States Department of Energy by National Technology & Engineering Solutions of Sandia, LLC.

Available to DOE and DOE contractors from
U.S. Department of Energy
Office of Scientific and Technical Information
P.O. Box 62
Oak Ridge, TN 37831

Telephone: (865) 576-8401
Facsimile: (865) 576-5728
E-Mail: reports@osti.gov
Online ordering: http://www.osti.gov/scitech

Available to the public from
U.S. Department of Commerce
National Technical Information Service
5301 Shawnee Rd
Alexandria, VA 22312

Telephone: (800) 553-6847
Facsimile: (703) 605-6900
E-Mail: orders@ntis.gov
Online order: https://classic.ntis.gov/help/order-methods/

ABSTRACT

Quantifying in-situ subsurface stresses and predicting fracture development are critical to reducing risks of induced seismicity and improving modern energy activities in the subsurface. In this work, we developed a novel integration of controlled mechanical failure experiments coupled with microCT imaging, acoustic sensing, modeling of fracture initiation and propagation, and machine learning for event detections and waveform characterization. Through additive manufacturing (3D printing), we were able to produce bassanite-gypsum rock samples with repeatable physical, geochemical and structural properties. With these "geo-architected" rock, we provided the role of mineral texture orientation on fracture surface roughness. The impact of poroelastic coupling on induced seismicity has been systematically investigated to improve mechanistic understanding of post shut-in surge of induced seismicity. This research will set the groundwork for characterizing seismic waveforms by using multiphysics and machine learning approaches and improve the detection of low-magnitude seismic events leading to the discovery of hidden fault/fracture systems.

ACKNOWLEDGEMENTS

This work was supported by the Sandia National Laboratories Laboratory Directed Research and Development program, Project No. 200180. We appreciate triaxial experimental testing from R. Charles Choens (08864), machine learning applications from Daniel Lizama (08864) and Rachel Willis (summer intern), SEM imaging from Jennifer Wilson, three point-bending testing from Liyang Jiang at Purdue University, and technical review from Courtney Herricks (08864). We also thank Moo Lee (08864) for his advice and support with project management.

CONTENTS

LIST OF FIGURES

LIST OF TABLES

This page left blank

ACRONYMS AND DEFINITIONS

Abbreviation	Definition
AE	Acoustic emission
ANN	artificial neural network
CNN	Convolutional Neural Network
CG	casted gypsum
CT	computed tomography
CV	cross-validation
EDX	energy dispersive x-ray spectroscopy
ETF	estimated time to failure
EQ	Earthquake
FFT	Fast Fourier Transform
KRR	Kernel ridge regression
LANL	Los Alamos National Laboratory
LightGBM	light gradient boosting method
LSTM	Short-Long Term Memory
LVDT	linear voltage displacement transducers
MAE	mean average error
NNs	neural networks
NSI	North Star Imaging Inc.
SEM	Scanning Electron Microscope
STA/LTA	short-term average / long-term average
UCS	uniaxial compressive strength
XGBoost	extreme gradient boosting method
XRD	X-ray diffraction

1. INTRODUCTION

Quantifying in-situ subsurface stresses and predicting fracture development are critical to reducing risks of induced seismicity and improving modern energy activities in the subsurface. In geologic formations, fluid injection or withdrawal causes changes in pore pressure, resulting in stress variations, hydraulic fracturing, fault (re-)activation, and/or fluid saturation changes. Typical continuum models employing simple Mohr-Coulomb theory are limited in their ability to account for mechanical discontinuities such as a fracture and/or fault system, and are unable to capture coupled geomechanical processes that can lead to fault (re-)activation and induced seismicity. Furthermore, crack initiation, propagation and coalescence of pre-existing discontinuities loaded in mixed mode I-II-III has remained virtually unexplored. In this research, we will develop a framework to use innovative "geo-architected" materials using additive manufacturing (i.e. 3D printing) and natural geologic specimens to investigate fracturing of rock subjected to controlled mechanical failure modes and improve our quantitative understanding of induced seismicity. An ambitious integration of seismic imaging experiments coupled with micro-CT imaging, modeling of fully coupled poroelastic processes during fluid injection, and machine learning techniques will allow us to (1) delineate fracture and failure mechanisms using well-controlled experiments with 3D printed geo-architected rocks, (2) determine poroelastic coupling mechanisms that lead to induced seismicity during fluid injection into subsurface, and (3) develop and apply machine-learning techniques for seismic wave data analysis and event detection.

2. MECHANICAL BEHAVIOR OF GEO-ARCHITECTED ROCK

2.1. Additive manufacturing of geo-architected rock

Powder-based additive manufacturing (i.e. 3D printing) was used to make "geo-architected rock" samples using commercially available bassanite powder (calcium sulfate hemihydrates, CaSO4·0.5H2O). In this work a commercial 3D printer (ProJet 360) was used to build a 3D structure of geo-architected samples by depositing a thin layer (100 microns) of bassanite powders onto build chamber. A print head (HP11 Printhead) dispenses a binder material (VisiJet PXL Clear Binder) with a specified binder amount as designed in Figure 2-1. This process is repeated by lowering the build chamber while providing a thin layer of fresh powders. The build bed area as shown in Figure 2-1 is ~20-30 cm.

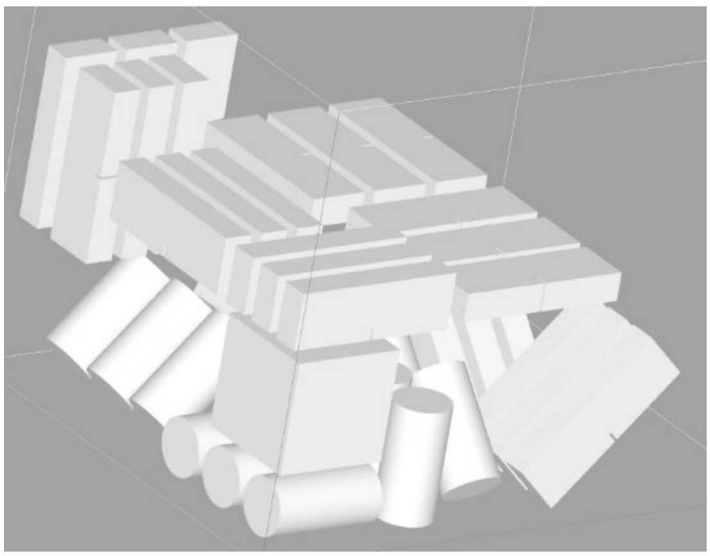

Figure 2-1. An example of 3D printing design. Cylinder samples in five different directions and 3 point-bending samples in 8 different directions are shown. To minimize the sample-sample variability, a batch of samples was printed together.

Calcium sulfate can exist in various structural forms with three distinct crystalline phases depending on the degree of hydration such as gypsum (dihydrate, $CaSO_4 \cdot 2H_2O$), bassanite (hemihydrate, $CaSO_4 \cdot 0.5H_2O$), and anhydrite (anhydrous, $CaSO_4$) (Van Driessche et al. 2017). 3D printing process is a reactive crystallization process from bassanite to a hydrated form of calcium sulfate (i.e., gypsum) when bassanite is in contact/mixed with the water-based solution as $CaSO_4 \cdot 0.5H_2O + 1.5H_2O = CaSO_4 \cdot 2H_2O$. Although this 3D printing process was used to construct the mechanical testing samples in the literature (e.g. Bobby 2014; Fereshtenejad and Song 2016; Jiang et al. 2016; Ju et al. 2017), a fundamentally mechanistic approach was not taken to investigate how reactive recrystallization process can give rise to distinctive mechanical properties depending on the printing layering and texture.

To observe the morphology of samples before and after 3D printing, a TESCAN Vega3 Scanning Electron Microscope (SEM) was used. Samples were mounted on sample stubs and sputter-coated with gold-palladium. Secondary electron (SE) images were collected at an accelerating voltage of 20.0 kV. The SEM images in Figure 2-2 show that powder sizes have a range of ~0.5 μm to 50 μm and small particles/thin plates are also attached to the surface of large particles. Elemental analysis of bassanite powders (weight %) using energy dispersive x-ray spectroscopy (EDX) in nine locations in Figure 2-2 is reported in Table 2-1. A majority of powders (~ 97% by weight) before the printing were reported as bassanite based on the X-ray diffraction (XRD) analysis (Jiang et al., 2019c); hence calcium sulfate phase can be interpreted as bassanite. Interestingly a high fraction of carbon was observed in several locations (Table 2-1) where SEM analysis shows this high carbon area is thin-white sheet-like precipitates as shown in Figure 2-2(b). Although it is not possible to originate this carbon source, it may come from bassanite production (e.g., Fukugaichi and Matsue 2018) or unknow inorganic carbonate impurities.

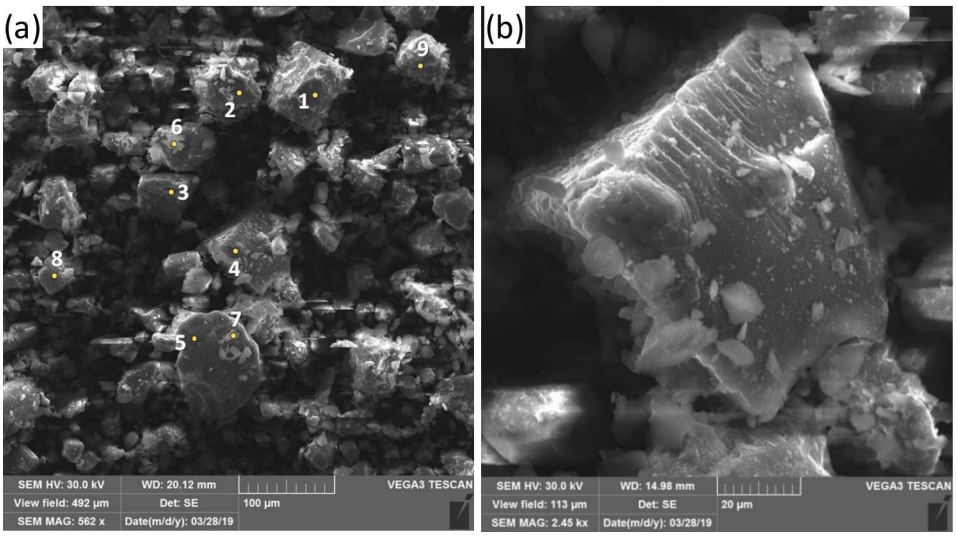

Figure 2-2. (a) Scanning electron microscope (SEM) images of bassanite powders and (b) high resolution image of Area 4 in (a). Nine areas located in (a) were used for elemental mapping and results are presented in Table 2.1.

Table 2-1. Elemental analysis of bassanite powders (weight %) using energy dispersive x-ray spectroscopy. Locations of selected area is shown in Figure 2-2(a).

Element	Area 1	Area 2	Area 3	Area 4	Area 5	Area 6	Area 7	Area 8	Area 9
C K	14.80			42.41		38.14	47.59		
O K	42.79	29.75	42.73	55.69	45.01	46.87	37.43	67.81	30.19
S K	16.98	25.22	23.07	0.31	22.13	6.12	6.29	15.16	22.43
CaK	24.56	43.38	34.20	1.01	32.86	7.54	8.64	30.30	44.81
AuL	0.87	1.65							0.35
NaK						1.34			

It has been studied to account for gypsum precipitation and growth from bassanite precursor phase (Van Driessche et al. 2012, 2017), while the presence of salts and organic components (e.g., 2-pyrrolidone, polyvinyl-pyrrolidone, or carboxylic acids) in the solution has an impact on the reaction

rates and mechanical strength (Polat and Sayan, 2017). Figure 2-3 shows SEM images of reactive recrystallization products that were formed after binder solution infiltrated into bassanite powders. Compared to original bassanite powders (Figure 2-2), the morphology of final reaction products is dramatically different. Elongated, well-faceted gypsum crystals structure is highly likely to be transformed from the oriented bassanite aggregates that were formed once water in binder solution reacted with bassanite powders as observed in the literature (Van Driessche et al., 2012). As shown in Figure 2-3, most of regions show elongated gypsum crystals with individual unreacted bassanite powders, however, the morphology along the boundary of the reactive product (not shown here) shows the partially covered reaction products with original powders. Since binder solution penetration ceased along the boundary, this reveals that solution infiltration through powder layers would impact the morphology of the 3D printed samples. Interestingly thin plates with high carbon contents (Figure 2-3c) did not undergo the chemical reaction, which indicates that these high carbon materials are not bassanite nor calcite minerals.

Although there is no systematic study in our work of the impact of salts and a major binder component (2-pyrrolidone) on 3D printing process, the previous studies show that these components impact the rock strength, hence failure surface roughness. Figure 2-3 also shows that the aggregation led to a morphological control that ultimately formed the large gypsum solid through the recrystallization. Lastly, the transformation of the hemihydrate bassanite to the dihydrate gypsum indicates that water must play an important role in the formation of bassanite nanorods and their ultimate material strength. The XRD measurement found that the printed samples (i.e. after application of the binder) were approximately 50-50 bassanite and gypsum, respectively, compared to a 97% bassanite in powders (Jiang et al. 2019c).

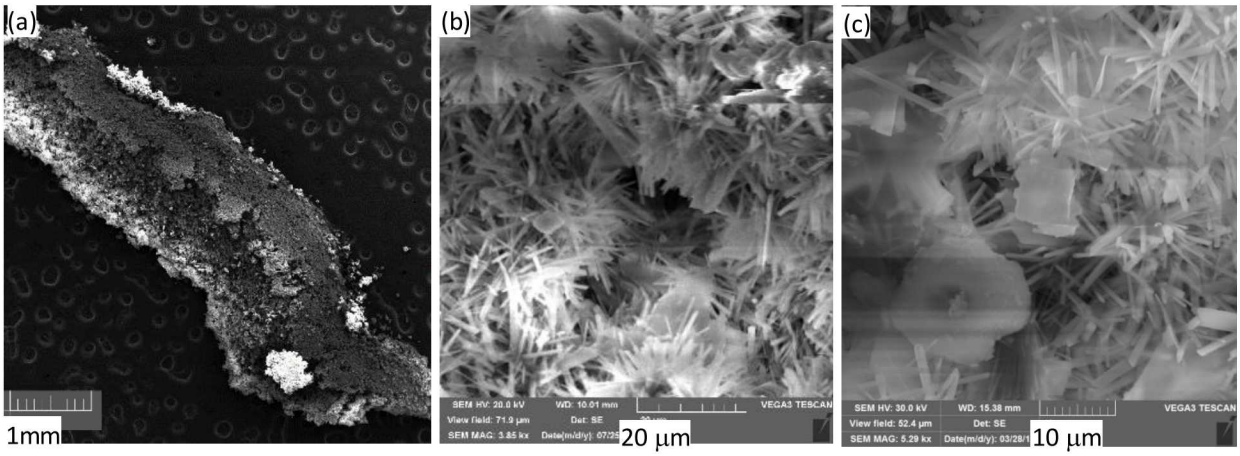

Figure 2-3. (a) Scanning electron microscope (SEM) image of a solid powder after reaction with a binder solution, (b) SEM image of rod shape gypsums, and (c) a mix of rod shape gypsum and unreacted thin plates

Special features such as cracks or flaws were printed at ~1mm feature resolution as shown in Figure 2-4. To evaluate the quality of printed samples, the X-Ray images were obtained using a North Star Imaging Inc. (NSI) X50 computed tomography (CT) scanning tool as described in our previous work (Martinez et al. 2017). This tool is equipped with a Fein Focus FXT-225.48-3 VER.FXE 225 KV / 3 MA X-Ray Source. A Varian Medical Systems PaxScan®2520DX Digital Image Receptor was used as the X-Ray detector. Image acquisition software utilized was NSI efx-dr as well as NSI efx-ct software for CT reconstruction (microCT images). Typical imaging was taken utilizing a 220 KV-Vortex scan with a voxel (resolution) size of ~ 18 microns. The vortex scan was performed by simultaneously taking X-Ray images while rotating and translating the sample under investigation in a helical path. Typical scan parameters would include taking ~8640 images while the sample is rotating ~ 8640 degrees (24 revolutions) concurrent with a z translation of 54 mm. Two examples of microCT images are shown in Figure 2-4b. These samples were printed with a default setting of the ProJet 360 to spray the binder at 100% saturation. However, the binder amount at the default mode for the shell area (i.e. outer boundary of the sample) was twice higher than that inside the core, hence the microCT intensity in the outer shell was higher (i.e. lighter gray) than that in the core due to a higher attenuation through the dense region. This uneven amount of the binder also affected the mechanical properties as shown in Figure 2-4c where the outer shell was easily peeled off after the failure. Hereinafter, we used the same binder amount for the entire volume of the samples.

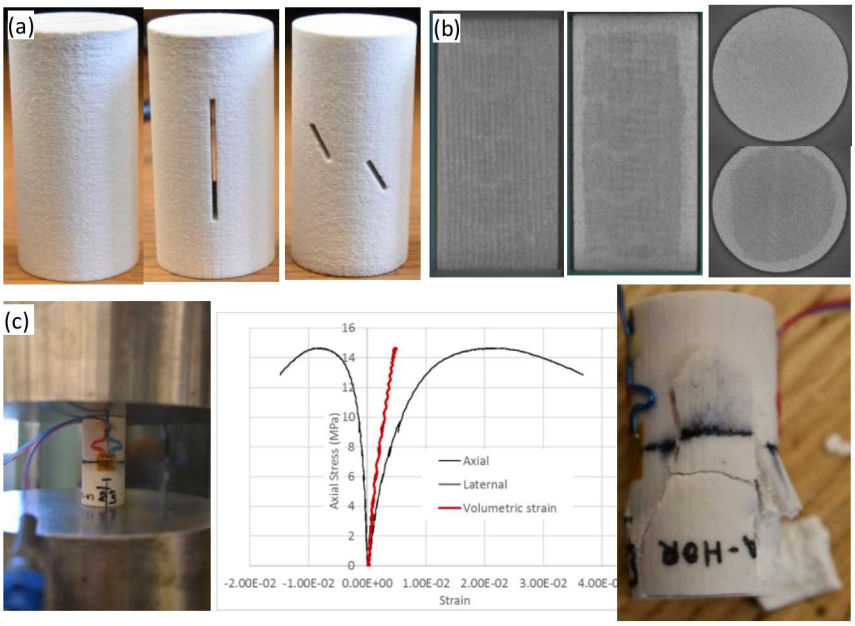

Figure 2-4. (a) Examples of 3D printed cylinder samples (1" diameter and 2" height), (b) microCT images of 3D printed samples (left: vertically layered sample, middle: horizontally layered sample, right: horizontal image slices of horizontally layered sample at the top and in the middle, and (c) unconfined strength testing setup, testing results, and photo of failure sample.

2.2. Material characteristics and mechanical testing of geo-architected samples

3D printed rocks were measured for dimensions, weights, acoustic velocities, porosity, and pre-photo before testing. P and S velocities were recorded with a Teledyne Lecroy Waveace 2024 oscilloscope and Olympus 5058PR pulser-receiver. Dimensions and acoustic velocities were measured at least 4 times per sample both laterally and axially along the parallel and perpendicular to the printed bedding (i.e. layering direction). For selected samples, a porosimetry device with helium gas was used to measure pore volume, so the porosity value of ~40% was consistently measured. Two linear voltage displacement transducers (LVDTs) in both the parallel and perpendicular printing direction were used for strain measurement for mechanical testing purposes. A small button for transducers was created out of small screws that were then milled to fit the curvature of the sample. A 5-minute epoxy was used to attach transducer buttons onto samples. The uniaxial compressive strength (UCS) test was conducted for the instrumented samples using an MTS 22,000lbf load frame. An MTS extensometer was also used to get a more accurate axial displacement recording. Testing was conducted in the displacement control at 0.000075in/s until the sample yielded. After the sample was tested, post-photos were taken. Buttons were removed from the samples and microCT scan was performed for several samples to obtain 3D images of the failure surfaces. In this work a cylindrical shape of rock testing samples was used for UCS testing and a small rectangular box shape of the samples was used for the three-point bending testing. Testing specimens are used to evaluate the effects of printing direction, the presence of flaws, and flaw geometry on the UCS and stress-strain behavior (Williams et al. 2017).

2.3. Impact of mineral texture on fracture geometry in layered geo-architected rock

The Influence of printing direction and mineral texture on fracture propagation and geometry was extensively investigated in Jiang et al. (2019b, 2019c) and Pyrak-Nolte et al. (2019). Here we briefly highlight he importance of our goals and key results while the interesting readers will be able to access the detailed information from Jiang et al. (2019b, 2019c) and Pyrak-Nolte et al. (2019). This work identifies a fundamental link between micro-scale mineralogy and fluid flow through fractures to evaluate the effect of compositional and structural heterogeneity on chemical and physical processes, which can aid in the modeling, design and monitoring of subsurface processes in rock. In natural rocks numerous previous works have tried to connect fracture flow path geometry and the failure strength of rock to layer orientation but experiments on natural rock have produced conflicting results. Complications arise from the inability to obtain natural rock samples with repeatable physical and chemical properties, even from the same rock mass (e.g. Na et al. 2017; Yoon et al. 2019). Through additive manufacturing (3D printing), we have produced bassanite-gypsum rock samples with repeatable physical, geochemical and structural properties. With these "geo-architected" rock, we provided the first demonstration of the role of mineral texture orientation on fracture surface roughness. This unique correspondence between the fracture geometry and the relative orientation of layers and mineral texture in rock can open the door to accurate prediction of fluid flow anisotropy. This advance impacts a wide range of geoscience applications with important societal impact, including the sustainability of geothermal systems, contaminant remediation, long-term subsurface storage of anthropogenic waste (CO_2, radioactive waste) and subsurface recovery and storage of energy fluids (oil & gas). This work demonstrated that mineralogical studies of mineral texture/fabric in laboratory samples is important to unraveling the preferential fracture flow paths in layered geological media.

3. EFFECT OF POROELASTIC COUPLING MECHANISMS ON INDUCED SEISMICITY BY FLUID INJECTION

Injection of large amounts of fluid into the subsurface alters the states of pore pressure and stress in the formation, potentially inducing human-made earthquakes. Considering full poroelastic coupling of pore pressure and stress, the earthquake occurrence after shut-in can be driven by primarily two mechanisms: (1) post shut-in diffusion of pore pressure into distant faults and (2) poroelastic stressing caused by fluid injection (e.g. Chang et al., 2018; Chang and Yoon 2018). The recent increase of induced seismicity has been linked to subsurface energy activities such as wastewater re-injection into the subsurface related to unconventional oil and gas development (Keranen et al. 2014; Keranen and Weingarten 2018), geothermal energy production (Giardini 2009), and geological CO_2 sequestration (White and Foxall 2016). Interactions of these mechanisms in the subsurface can depend on several key factors including fault geometry, hydraulic and mechanical properties of the formation, and injection operation. In this project, we evaluated the poroelastic coupling mechanisms related to induced seismicity caused by key subsurface energy activities listed above.

First, three-dimensional (3D) model system consisting of the upper caprock, reservoir, and basement intersected by vertical strike-slip faults was used to evaluate the hydraulic and mechanical interaction between faults and surrounding formations (Chang and Yoon 2018). This first case was a general setup related to the poroelastic coupling processes encountered by fluid injection into the subsurface, although this case can be more related to wastewater reinjection from unconventional resources recovery. The full poroelastic behavior of the formation and the mechanical response along the fault zone under representative fluid injection scenarios were investigated using the Coulomb stress change. The spatio-temporal distributions of stresses and pore pressure was then used to predict the magnitude, rate, and location of potential induced seismicity. Simulation results demonstrate that direct diffusion of pore pressure destabilizes conductive faults, potentially inducing most frequent seismicity with large magnitudes. Less permeable faults can be destabilized by poroelastic stressing or delayed pore-pressure diffusion. A two-dimensional (2D) horizontal model, representing the interface between the reservoir and the basement, limits diffusion of pore pressure and deformation of the formation in the vertical direction that may over- or under-estimate the potential of earthquakes along the fault. Our simulation results suggest that the 3D modeling of faulting system including poroelastic coupling is required to properly predict the seismic hazard along the faults by considering the hydraulic and mechanical interaction between faults and bounding formations. The detailed model setup and discussion is provided in Chang and Yoon (2018).

Second, a 2D aerial view of the reservoir formation intersected by strike-slip basement faults was used to evaluate the impact of injection-induced pressure buildup on seismicity rate surge (Chang and Yoon 2019). The same mechanical model used in Chang and Yoon (2018) was used with a slight modification. A series of sensitivity tests were developed to mimic CO_2 injection scenarios by considering the variation in (1) permeability of the fault zone, (2) the locations and number of faults with respect to the injector, and (3) well operations with time-dependent injection rates. Simulation results show that lower permeability faults such as the basement bedrock underneath the reservoir formation can have higher seismicity potential than more permeable faults after shut-in due to delayed diffusion and poroelastic stressing. Hydraulic barriers, depending on their relative location to injection, can either stabilize or weaken a conductive fault via poroelastic stresses. Gradual reduction of the injection rate minimizes the Coulomb stress change and the least seismicity rates were predicted due to slower relaxation of coupling-induced compression as well as pore-pressure

dissipation. In the multiphase flow system, the contrast of fluid and rock properties between different structures produces the changes in pressure gradients and subsequently stress fields. Assuming two-phase fluid flow (gas-water system) and poroelasticity, we simulated the three-layered formation including a basement fault, in which injection-induced pressure encounters the fault directly given injection scenarios (Chang et al., 2019). The single-phase poroelasticity model with the same setting was also used to evaluate the multiphase flow effects on poroelastic response of the fault to gas injection. Simulation results show that the presence of gaseous phase tends to reduce the pressure buildup within the highly gas-saturated region, causing less Coulomb stress changes, whereas capillarity increases the pore pressure within the gas-water mixed region. Even though the gaseous plume does not approach the fault, the poroelastic stressing can affect the fault stability, potentially the earthquake occurrence.

Third, the coupled fluid flow and geomechanical model used above has also been applied to develop a conceptual model of the primary processes that can induce seismicity related to fluid injection during enhanced geothermal activity. In particular, we constructed our numerical model to simplify the geothermal system in Pohang, South Korea where the pilot test of enhanced geothermal operations triggered a Mw 5.5 earthquake (e.g. Kim et al. 2018; Lee et al. 2019). Given field operational conditions and previous studies to develop a fault zone conceptual model, our simulation results show that poroelastic stressing can perturb the stress state on the fault beyond the effect of direct pore-pressure elevation, and alternating injection-extraction operations at either side of the fault plane could enhance the efficacy of pore-pressure diffusion through the low permeability basement. The combined effect of poroelastic shearing and delayed pore-pressure accumulation can cause slip on a preexisting fault, potentially inducing the post shut-in Mw 5.5 Pohang earthquake.

4. MACHINE LEARNING APPLICATIONS FOR LABORATORY GEOPHYSICAL DATA DURING FAILURE MECHANICAL TESTING

4.1. Earthquake prediction based on a laboratory test

A research team led by a Los Alamos National Laboratory team organized Google's Kaggle competition on "LANL Earthquake Prediction" (LANL 2019). The objective of the competition was to improve earthquake (EQ) forecasting using various machine learning methods about when, where, and how large the EQ will be. The laboratory testing was previously performed in a bi-axial testing (Rouet-Leduc et al. 2017) where continuous acoustic waveform data has been obtained during a total of 16 direct shear failure events as shown in Figure 4-1. The training data was a single continuous dataset containing 16 aperiodic earthquake events with known estimated time to failure (ETF), while the testing data consisted of over 2,000 data files of unknown EFT seismic sequence with 150,000 data-points each. In this study we primarily focused on exploring machine learning architectures that can answer the time of EQ event.

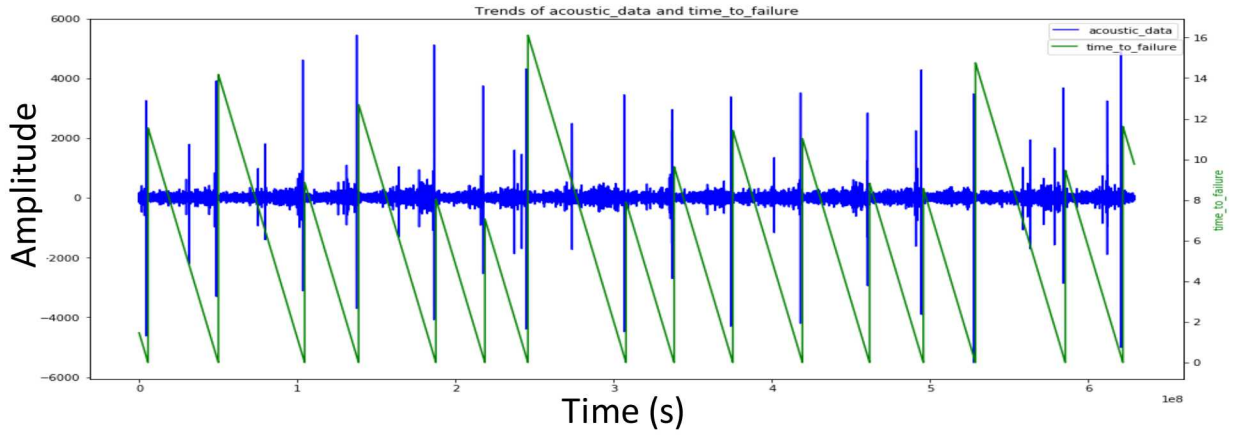

Figure 4-1. Acoustic signal of 16 shear slip events over time and time to failure to each failure event. Plotted from training data available in LANL (2019).

The data analysis was performed through a series of processes including pre-process, feature extraction, training, and prediction to improve EQ prediction. During pre-processing, the data has been modified by applying noise and subtracting the median to generalize or diversify the data and produce a smoother input space. Also, we may or may not want to apply digital filters to get rid of undesired signal artifacts corresponding to non-seismic activity. Regardless of the pre-processing, our main approach consists of segmenting the continuous training set into a window of 150,000 points long, corresponding to known ETF, which made training samples directly comparable to the testing data.

A feature extraction step entails quantifying the physical and statistical characteristics that describe the signal event. For example, Fast Fourier Transform (FFT) will describe the acoustic frequencies present in the signal (with corresponding energy), and the ratio of the short-term average to the long-term average (STA/LTA) will describe the difference in amplitude between short and long time windows. A list of common features includes mean, standard deviation, change rate, percentile, quantiles, trend regression, FFT, STA/LTA, correlation, kurtosis, skewness, energy, Mel-

frequencies, minimum, maximum, zero Crossing, number of peaks, medians, sum, autocorrelation, and difference. Features such as standard deviation, quantiles, Mel-frequencies, and autocorrelation yielded the best results at the final models. Usage of features instead of input signal generalizes the problem given that similar signals will have approximate values and dissimilar ones will not. A feature correlation analysis shows a significant amount of features to be highly correlated as shown in Figure 4-2a. Reducing redundant features with high correlations generally increased prediction accuracy. It is noted that the relevancy of each feature depends on the architecture of the machine learning model. Practically, maintaining only the top ranked features tend to increase the prediction accuracy.

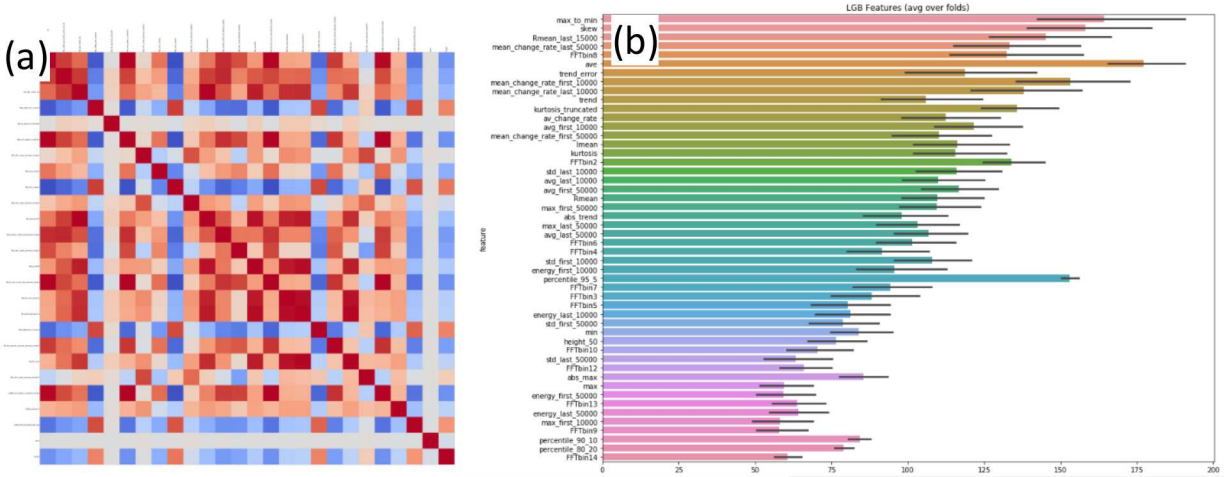

Figure 4-2. (a) An example of feature correlation with high and low correlations in red and blue, respectively, and (b) The rank of feature importance with light gradient boosting method (LightGBM). The features include mean, standard deviation, change rate, percentile, quantiles, trend regression, FFT, STA/LTA, correlation, kurtosis, skewness, Energy, Mel-frequencies, minimum, maximum, zero Crossing, number of peaks, medians, sum, autocorrelation, and difference.

Once feature sets were determined, these features can be used for the training process. Some of the machine learning methods tested are decision trees (light gradient boosting method (LightGBM), extreme gradient boosting method (XGBoost)), support vectors (Support Vector Regressor, Kernel Ridge Regression), and neural networks (NNs) (artificial neural network (ANN), Short-Long Term Memory (LSTM), Convolutional Neural Networks (CNNs)). Each method was trained and then tested to produce a single prediction for each testing dataset. The output corresponded to a predicted ETF of an EQ for each of the testing data files, which is then tabulated and submitted into the competition for accuracy analysis. The accuracy of the model was measured by the mean average error (MAE). It defines the average difference between the predicted and true values, meaning that lower scores are better. Most scores in the competition fell between 2.3 (winner) and 2.7 seconds as the MAE.

In the competition the performance accuracy was evaluated with "blind" data set while during the competition a certain data set was used to evaluate the performance of participants' progress. We evaluated cross-validation (CV) measures and the accuracy with the public data. We tested various sets of features and evaluated other top ranked algorithms in the competition (LANL, 2019). The

interesting readers can find the data and algorithms posted in the competition website. Here, we briefly discuss some results of mixing and matching features and models. In the first case all 64 features considered were used to compare results of two decision tree methods (LGB and XGB). The LGB result was similar to the XGB result (2.66 vs. 2.67), although both scores were close to the lowest rank in the competition. It is noted that averaging each model's prediction resulted in a better score (2.65) than each model's performance. The same trend was observed with the reduced feature set based on the second place winner's algorithm. However, both LGB (2.7) and XGB (2.7) resulted in decreasing prediction accuracy. Although it is generally expected that reducing features would increase the accuracy, this exercise demonstrates that the significance of features selected also depends on the model architecture. The second model was modified by adding features used in the first place winner's algorithm. Both LGB (2.65) and XGB (2.64) with this combined feature set significantly increased the prediction accuracy compared to the second model, highlighting that that better features (for the given model) will increase the accuracy. Kernel ridge regression (KRR) was also incorporated into the analysis in this model and resulted in the better score (2.525) than other methods. Lastly, the fourth model incorporates the least features by only using the most relevant features described by the first and second place algorithms. This resulted in the best score (2.521) among the models tested in this work This comparison indicates that a reduced number of features with the highest relevance are a key to improve the prediction accuracy.

It's noted that some of the features are highly relevant in most models. In addition, averaging of multiple model predictions could improve the performance score in most cases. Typically, models with less parameters yield better accuracy with faster tuning time. Overall, predictions over 10 seconds long for the time to failure can be made with an average error of 2.5 seconds based on this work.

4.2. Sensing of Fracture Systems Using Elastic Waves from Induced Seismicity

Induced and natural seismicity generate seismic events that vary in magnitude and spectral content depending on the focal mechanism and amount of slip. These event features are most often used to locate the source of the seismic event and to interpret the magnitude of fault displacement and the orientation of the local stress field. While this is important for identifying the source of seismicity (e.g. hydraulic fracturing, faults, fluid production), most of the other information content in seismic waves goes unused. Induced seismicity provides a set of events (where each event has unique spectral content) that acts as a stochastic broadband source for characterization of existing fractures. Here we planned to exploit the information content of seismic events to interpret the mechanical properties of fractures that are not associated with the seismic event, i.e. at some other location in the reservoir similar to using ambient noise for imaging (e.g. Hillers and Campillo 2016).

As described in the Section 2, we performed laboratory experiments on 3D printed rock to generate acoustic emissions under controlled loading conditions (Jiang et al. 2019a). Uniaxial compressive strength (UCS) tests monitored with six broadband AE transducers were performed with cylindrical specimens: casted gypsum (CG) samples, and 3D printed (3DP) samples with five different orientations of bassanite layer and gypsum texture relative to the loading direction. UCS varied by 150% among the samples, primarily due to anisotropy in the 3DP samples. Unlike the CG samples, no axial splitting was observed from the 3DP samples, and a single inclined (relative to loading direction) major crack was observed instead. The fracture location estimated by AE localization technique was comparable to that observed from microCT images. CG samples failed immediately after reaching a peak load, while 3DP samples exhibited ductile post-peak behavior. Examination of the AE signal amplitude from post-peak loading revealed that more ductile behavior was associated with more AE events that occurred over a longer period of time, and the resultant fracture surfaces were rougher than for narrow distributions. Monitoring of AE signals during failure of rock has the potential to predict fracture roughness and the mineral and layering patterns. We plan to apply feature selection algorithms described in the Section 4.1 and fingerprinting selection methods (Yoon et al. 2015; Holtzman et al. 2018).

5. CONCLUSIONS

This project provided a novel integration of controlled mechanical failure experiments coupled with microCT imaging, acoustic sensing, modeling of poroelastic coupling processes, and machine learning for event detections and waveform characterization. It is currently difficult to detect low-magnitude, unidentified seismic events and locations used to discover hidden fault or fracture systems in the earth's crust with great accuracy. Discovery of these unknown or hidden fault systems can lead to predictions of the magnitudes, rates and locations of potential earthquakes when monitored properly. Through the academic alliance partnership with researchers at Purdue University we were able to create new methods for sensing of rock failures by inducing seismic activity using 3D printed samples under controlled mechanical failures and identifying the signatures of these events. The framework developed through this project will be able to integrate experimental, numerical, and data analysis in order to link mechanical discontinuities, fracture mechanics, and pore pressure or stress to the geophysical signatures identified in both laboratory and field scenarios.

The controlled laboratory work was used to learn the geomechanical and geophysical mechanisms that can be applicable for the field scale problem. In particular, this approach can be realized through machine learning techniques that have a potential to extract the spatial variation in the interpretation of source spectral content related to fractures or fracture systems. The displacement discontinuity theory (also known as linear slip) and laboratory experiments have shown that fractures behave as low past filters with a characteristic frequency related to the impedance of the rock matrix and the stiffness of the fracture. For a known fracture stiffness, the time delay, and transmission and reflection coefficients are frequency dependent. The integrated approach with the geo-architected rocks with various fracture features, AE acquisitions, and forward physical modeling can help us to validate that AE events vary in magnitude and hence spectral content. It is this variation in spectral content that will provide a fundamental tool for characterizing remote fractures because the amount of attenuation and signal delay in regions with fractures will be frequency dependent. During this 3-year project our technical accomplishments can be listed as:

1. Through additive manufacturing (3D printing), we were able to produce bassanite-gypsum rock samples with repeatable physical, geochemical and structural properties. With these "geoarchitected" rock, we can provide the first demonstration of the role of mineral texture orientation on fracture surface roughness. This unique correspondence between the fracture geometry and the relative orientation of layers and mineral texture in rock opens the door to accurate prediction of fluid flow anisotropy and mechanistical link between geomechanics and geophysical signature. This work was submitted for the journal publication as Jiang et al. (2019c).
2. The impact of poroelastic coupling on induced seismicity has been systematically investigated to improve mechanistic understanding of post shut-in surge of induced seismicity using two primary mechanisms of pore pressure diffusion and poroelastic stressing. This mechanistic approach has been applied for subsurface energy applications such as wastewater injection related to unconventional resources recovery (Chang and Yoon 2018), geologic CO_2 storage (Chang et al. 2019a; Chang and Yoon 2019), and geothermal resource recovery (Chang et al. 2019b).
3. A workflow to integrate multi-imaging, geophysical sensing (p- and s-waves, acoustic emission), and geomechanical testing was established to delineate in-situ signatures of induced seismicity. This new capability will benefit us to accomplish high resolution geophysical sensing under natural and extreme conditions during geomechanical testing.

4. Various machine learning methods with feature selections based on the laboratory data were evaluated, which can be validated to apply for more realistic field scale data analysis with forward/inverse modeling approach for integrated geomechanical and geophysical sensing.

Finally, the outcome of this project can lead us to analyze the geophysical and mechanical data using various machine learning techniques for event detection, waveform similarity-based event detection, and template matching. As a result of this research, additive manufacturing applications will be set to be used for more broad themes in the future. This research will set the groundwork for characterizing seismic waveforms by using multiphysics and machine learning approaches and improve the detection of low-magnitude seismic events leading to the discovery of hidden fault/fracture systems.

REFERENCES

[1] Bobby, S.S. 2014. "A preliminary investigation of gypsum bonded moulds by three dimensional printing." *Int. J. Res. Eng. Technol, 3(06)*, pp.501-507.

[2] Chang, K.W. and Yoon, H., 2018. "3-D Modeling of Induced Seismicity Along Multiple Faults: Magnitude, Rate, and Location in a Poroelasticity System." *Journal of Geophysical Research: Solid Earth, 123(11)*, pp.9866-9883.

[3] Chang, K.W., H. Yoon, M.J. Martinez, and P. Newell. 2018. "Coupled multiphase flow and geomechanical modeling of injection-induced seismicity." *The 52nd US Rock Mechanics/Geomechanics Symposium.* **[Conference]**

[4] Chang, K. W. and Yoon, H., "Impact of basement fault characteristics on the patterns of injection-induced seismicity." (Submitted to Earth and Planetary Science Letters), 2019. **[Submitted]**

[5] Chang, K.W., H. Yoon, M.J. Martinez, and P. Newell. 2019a. "Coupled hydro-mechanical modeling of injection-induced seismicity in the multiphase flow system." *The 53rd US Rock Mechanics/Geomechanics Symposium.* **[Conference]**

[6] Chang, K.W., Y. Kim, M.Y. Lee, and H. Yoon. "Physical mechanisms inducing the 2017 Mw 5.5 Pohang earthquake." (Submitted to Proceedings of the National Academy of Sciences), 2019b. **[Submitted]**

[7] Fereshtenejad, S. and Song, J.J. 2016. "Fundamental study on applicability of powder-based 3D printer for physical modeling in rock mechanics." *Rock Mechanics and Rock Engineering, 49(6)*, pp.2065-2074.

[8] Fukugaichi, S. and Matsue, N. 2018. "One-Step Synthesis of Calcium Sulfate Hemihydrate Nanofibers from Calcite at Room Temperature." *ACS Omega, 3(3)*, pp.2820-2824.

[9] Giardini, D. 2009. "Geothermal quake risks must be faced." *Nature, 462*, 848–849. https://doi.org/10.1038/462848a.

[10] Hillers, G. and M. Campillo. 2016. "Fault zone reverberations from cross-correlations of earthquake waveforms and seismic noise." *Geophysical Journal International, 204 (3)*. 1503-1517. https://doi.org/10.1093/gji/ggv515.

[11] Holtzman, B.K., Paté, A., Paisley, J., Waldhauser, F. and Repetto, D. 2018. "Machine learning reveals cyclic changes in seismic source spectra in Geysers geothermal field." *Science advances, 4(5)*, p.eaao2929.

[12] Jiang, C., Zhao, G.F., Zhu, J., Zhao, Y.X. and Shen, L. 2016. "Investigation of dynamic crack coalescence using a gypsum-like 3D printing material." *Rock mechanics and rock engineering, 49(10)*, pp.3983-3998.

[13] Jiang, L., Yoon, H., Bobet, A., and Pyrak-Nolte, L. 2019a. "Monitoring Fracture Formation in Additively Manufactured Anisotropic Rocks." *International Institute of Innovative Acoustic Emission*, Chicago, USA, June 17-20, 2019. **[Conference]**

[14] Jiang, L., Yoon, H., Bobet, A., and Pyrak-Nolte, L. 2019b. "Effect of Mineral Orientation on Roughness and Toughness of Mode I Fractures." *The 53rd US Rock Mechanics/Geomechanics Symposium, 19-A-483*, New York, June 2019. **[Conference]**

[15] Jiang, L., Yoon, H., Pyrak-Nolte, L., and Bobet, A. "The Influence of Mineral Texture on Fracture Geometry in Layered Geo-Architected Rock." (Submitted to Nature Geoscience), 2019c. **[Submitted]**

[16]Ju, Y., Wang, L., Xie, H., Ma, G., Zheng, Z. and Mao, L. 2017. "Visualization and transparentization of the structure and stress field of aggregated geomaterials through 3D printing and photoelastic techniques." *Rock Mechanics and Rock Engineering, 50(6)*, pp.1383-1407.

[17]Kim, K.H., Ree, J.H., Kim, Y., Kim, S., Kang, S.Y. and Seo, W. 2018. "Assessing whether the 2017 Mw 5.4 Pohang earthquake in South Korea was an induced event." *Science, 360(6392)*, pp.1007-1009.

[18]Keranen, K. M., Weingarten, M., Abers, G. A., Bekins, B. A., & Ge, S. 2014. "Sharp increase in central Oklahoma seismicity since 2008 induced by massive wastewater injection." *Science, 345*, 448–451. https://doi.org/10.1126/science.1255802.

[19]Keranen, K.M. and Weingarten, M., 2018. "Induced seismicity." *Annual Review of Earth and Planetary Sciences, 46*, pp.149-174.

[20]LANL, 2019. LANL-Earthquake-Prediction. https://www.kaggle.com/c/LANL-Earthquake-Prediction/. Accessed 7/29/2019.

[21]Lee, K.K., Ellsworth, W.L., Giardini, D., Townend, J., Ge, S., Shimamoto, T., Yeo, I.W., Kang, T.S., Rhie, J., Sheen, D.H. and Chang, C. 2019. "Managing injection-induced seismic risks." *Science, 364(6442)*, pp.730-732.

[22]Ligon, S.C., Liska, R., Stampfl, J., Gurr, M. and Mülhaupt, R., 2017. "Polymers for 3D printing and customized additive manufacturing." *Chemical reviews, 117(15)*, pp.10212-10290.

[23]Martinez, Mario J., Hongkyu Yoon, Alec Kucala, Thomas Dewers, and Hector Mendoza. 2017. Digital Rock Physics and 3D Printing for Fractured Porous Media. SAND2017-10469. Sandia National Laboratories. **[UUR]**

[24]Na, S., Sun, W., Ingraham, M.D. and Yoon, H. 2017. "Effects of spatial heterogeneity and material anisotropy on the fracture pattern and macroscopic effective toughness of Mancos Shale in Brazilian tests." *Journal of Geophysical Research: Solid Earth, 122(8)*, pp.6202-6230.

[25]Polat, S., Sayan, P. 2017. "Determination of the effects of carboxylic acids on calcium sulfate dihydrate crystallization." *Chemical Engineering & Technology, 40(7)*, 1354-1361.

[26]Pyrak-Nolte, L. Jiang, L., A. Modiriasari, Yoon, H., and Bobet, A. 2019. "Translating the Micro-scale to the Macro-Scale: Signatures of Fracture Evolution." *ISRM 2019*, Brazil, September, 2019. **[Conference]**

[27]Rouet-Leduc, B., Hulbert, C., Lubbers, N., Barros, K., Humphreys, C. J., & Johnson, P. A. 2017. "Machine learning predicts laboratory earthquakes." *Geophysical Research Letters*, 44, 9276– 9282.

[28]Van Driessche, A. E. S., Benning, L. G., Rodriguez-Blanco, J. D., Ossorio, M., Bots, P., García-Ruiz, J. M. 2012. "The role and implications of bassanite as a stable precursor phase to gypsum precipitation." *Science, 336(6077)*, 69-72.

[29]Van Driessche, A. E., Stawski, T. M., Benning, L. G., Kellermeier, M. 2017. "Calcium sulfate precipitation throughout its phase diagram." In *New Perspectives on Mineral Nucleation and Growth* (pp. 227-256). Springer, Cham, https://doi.org/10.1007/978-3-319-45669-0_12.

[30]White, J. A., and Foxall, W. 2016. "Assessing induced seismicity risk at CO2 storage projects: Recent progress and remaining challenges." *International Journal of Greenhouse Gas Control, 49*, 413–424.

[31]Williams, M., Yoon, H., Choens, R.C., Martinez, M.J., Dewers, T. and Lee, M.Y. 2017. Powder-Based 3D Printing Application for Geomechanical Testing. SAND2017-13305C. Sandia

National Laboratories (SNL-NM). **[UUR]** Available at https://www.osti.gov/servlets/purl/1486888.

[32]Yin, D.W., Chen, S.J., Liu, X.Q., Ma, H.F. 2018. "Simulation study on strength and failure characteristics for granite with a set of cross-joints of different lengths." *Adv. Civil Eng.*, 2384579.

[33]Pyrak-Nolte, L. J. and Nolte, D. D. 2016. "Approaching a universal scaling relationship between fracture stiffness and fluid flow." *Nature Communications, 7*, p.10663.

[34]Yoon, C.E., O'Reilly, O., Bergen, K.J. and Beroza, G.C., 2015. Earthquake detection through computationally efficient similarity search. *Science advances, 1(11)*, p.e1501057.

[35]Yoon, H., M. D. Ingraham, J. Grigg, B. Rosandick, P. Mozley, A. Rinehart, W. M. Mook, and T. Dewers. 2019. "Impact of Depositional and Diagenetic Heterogeneity on Multiscale Mechanical Behavior of Mancos Shale, New Mexico and Utah, USA." p.121-148. Chapter 8 in W. Camp, K. Milliken, K. Taylor, N. Fishman, P. Hackley, and J. Macquaker, eds., *Mudstone diagenesis: Research perspectives for shale hydrocarbon reservoirs, seals, and source rocks*: AAPG Memoir 120. **[In Press]**

This page left blank

DISTRIBUTION

Email—Internal

Name	Org.	Sandia Email Address
John Eric Bower	05232	jebower@sandia.gov
Kyung Won Chang	08862	kchang@sandia.gov
Moo Y. Lee	08864	mylee@sandia.gov
Michelle Williams	08864	mwilli9@sandia.gov
Hongkyu Yoon	08864	hyoon@sandia.gov
Technical Library	01177	libref@sandia.gov

This page left blank

This page left blank

Sandia National Laboratories

Sandia National Laboratories is a multimission laboratory managed and operated by National Technology & Engineering Solutions of Sandia LLC, a wholly owned subsidiary of Honeywell International Inc. for the U.S. Department of Energy's National Nuclear Security Administration under contract DE-NA0003525.